



Zn-free MOFs like MIL-53(Al) and MIL-125(Ti) for the preparation of defect-rich, ultrafine ZnO nanosheets with high photocatalytic performance

He Xiao^{a,b}, Wenyao Zhang^b, Qiushi Yao^d, Liulian Huang^a, Lihui Chen^a, Bruno Boury^{c,*}, Zhongwei Chen^{b,*}

^a College of Material Engineering, Fujian Agriculture and Forestry University, Fuzhou, 350108, China

^b Department of Chemical Engineering, University of Waterloo, Waterloo, Ontario N2L3G1, Canada

^c Institute Charles Gerhardt UMR CNRS 5253, CMOS team, Université de Montpellier, CC1701, place E. Bataillon, 34095, Montpellier, France

^d Department of Physics and Shenzhen Institute for Quantum Science and Technology, Southern University of Science and Technology, Shenzhen, 518055, China



ARTICLE INFO

Keywords:

Photocatalysis
Zinc oxide
MOFs
Template
Oxygen defects

ABSTRACT

Metal organic frameworks (MOFs) are exploited in many applications of materials science and very recently were investigated as precursors or reagents for material synthesis. In a new way different from previous approaches, here we introduce for the first time the synthesis of metal oxide M_xO_y in the presence of M-free MOF acting partially as a sacrificial template and as a provider of doping metal atom. We demonstrate this approach in the case of ZnO prepared by a simple hydrothermal method in the presence of a Zn-free MOF like MIL-53(Al) or MIL-125(Ti). The resulting ZnO show low content of Al or Ti < 2% and properties are significantly different depending on whether MIL-53(Al) or MIL-125(Ti) are used or if no MOF is present. The nature and presence of MOF has different major effects on the morphology, the specific surface area of as prepared ZnO and also on the oxygen defects in its crystal structure. Corroborating the XPS, UV-vis DRS, PL, EPR and DFT studies evidence the role of such O-defects on band gap narrowing for samples calcined at 400 °C. These exhibit high efficiency in photodegradation of methyl orange (MO) compared to ZnO prepared in MOF-free conditions or previous literatures. The kinetics of MO degradation is different depending on the morphology, the specific surface and oxygen defects. The present data open the door to a new approach of the synthesis of metal oxides and a control of their properties.

1. Introduction

One of the most realistic and efficient green solutions for the overwhelming energy and environmental crisis rely on photocatalytic processes. Diverse pollutants can be degraded into carbon dioxide and water [1,2], and from this point of view, zinc oxide is one of the common and attractive semiconductors. Due to its wide band gap ~3.3 eV, exciton binding energy of 60 mV, good thermal stability and chemical stability, ZnO has wide applications in photocatalysis [3–5], solar cells [6,7], gas sensors [8,9] and other fields [10,11].

The performance of such photocatalysts can be enhanced through optimizing micro- and nanostructuration to obtain high photon absorption, high specific area and efficient separation of charge carrier [12,13]. Photocatalysts with hierarchical structures are generally obtained through controlled assembling of primary particles into secondary structures generally with the aid of templates. Such hierarchical structure is important at different levels for photocatalytic reactions.

First, incident light repeatedly scattering on the surface of the multi-level structure can increase the absorption efficiency. Additionally, this may reduce charge-hole recombination and enhance their presence at the surface of the photocatalyst. Finally, a hierarchical structure from the macro to the microscale level is generally targeted to succeed in high specific surface area and therefore to increase the proportion of active catalytic sites. Various recent synthetic methods have been developed to prepare zinc oxide (ZnO) with hierarchical microstructures such as nanospheres [14], nanowires [15], nanoflowers [16], nanorods [17], etc.

In a continuous effort to find new ways of synthesizing materials and with the idea of producing materials with better performances, we have considered the synthesis of ZnO using Zn-free Metal Organic Frameworks (MOFs) like MIL-125(Ti) and MIL-53(Al), these latter being easily available and well-known hybrid coordination compounds combining metal centers and organic ligands with functional groups [18,19]. Because of the tremendous porosity that they can exhibit, the

* Corresponding authors.

E-mail addresses: bruno.boury@univ-montp2.fr (B. Boury), zwhchen@uwaterloo.ca (Z. Chen).

huge specific surface area and their regular structures, some of the MOFs have been applied in the field of adsorption [20], hydrogen storage [21], catalysis [22], etc.

MOFs themselves such as SMIL-NH₂ [23] and HKUST-1 [24], were checked as catalysts of the photodegradation of organic compounds in waste-water. Although they exhibit interesting performances in the photodegradation for water pollutants, however, they suffer of a severe limitation due to their instability under the acid or alkaline conditions [25,26]. Meanwhile, in order to enhance the adsorption performance during the photocatalytic reaction, MOFs had been loaded onto the surface of other photocatalysts [27,28]. More frequently, MOFs are the precursors of metal oxides; in the case of ZnO this third way consist in converting by a thermal or chemical process a Zn-containing MOF, specially MOF-5 and ZIF-8, leading to a pure ZnO or ZnO/C nanocomposites if pyrolysis is used [29–32]. With MOF-5 and ZIF-8 as Zn-sources, ZnO is grown as hetero-nanostructured nanocrystals with good efficiency in photocatalytic hydrogen production [33] and CO₂ reduction [34], respectively. In order to enhance the adsorption and photocatalytic activity, the precursor of Zn-based MOFs can be converted into C- or N-doped ZnO nanocrystals not only with high specific surface area, but also with inheriting the micromorphology of MOFs templates [27,35].

It is worthwhile to mention that, in an opposite route, metal oxide like ZnO can be used as an efficient nucleating agent and a source of metal cation, here Zn²⁺, to form highly oriented MOFs layers applied in catalyst [36,37], adsorbents [38], Zn-air battery [39], catalyst [40], etc. In all these previous reports on the preparation of ZnO from MOFs, the latter is the source Zn ions. Our approach is completely different, and to the best of our knowledge, it is not the subject of any previous reports. Here, we do not consider the MOFs as the Zn-source, but only as a template and a possible source of another metal, Al and Ti in the present case, as a potentially doping element of ZnO, as shown illustration of the general concept in Fig. 1. In addition, MOFs were introduced in very low quantity compared to the quantity of ZnO precursors. We found that MOFs, here MIL-125(Ti) or MIL-53(Al), are transformed by the process, at the same time that it provides a possible template and a source of other metal for the growth and/or doping of the ZnO. We also wanted to compare the effect of different MOFs on this ZnO process.

In comparison with the use of zinc acetate as ZnO precursor, we explore how ZnO grains growth can be controlled by the MOFs

structure that itself is slowly hydrolyzed in the alkaline condition. We found that the metal cation of the MOFs was sparingly incorporated into the ZnO nanocrystals. Several advanced techniques were applied to investigate the effect of MOFs templates on the properties of ZnO nanocrystals such as spectroscopy (FT-IR, Raman), XRD, N₂ adsorption, scanning electron microscopy (SEM), transmission electron microscope (TEM), etc. The photocatalytic activities of ZnO nanocrystals were evaluated for methyl orange degradation by a set of different and complementary studies.

2. Experimental

2.1. Materials

Terephthalic acid, aluminum nitrate nonahydrate Al(NO₃)₃·9H₂O, titanium(IV) n-butoxide Ti(O-(CH₂)₃–CH₃)₄, methyl orange (MO, 96%), methanol, ethanol, zinc acetate Zn(OCO–CH₃)₂, potassium hydroxide and N,N-Dimethylformamide (DMF) were purchased from Aladdin Industrial Corporation, China. DMF and methanol were distilled with calcium hydroxide before experiment in order to remove residual water and stored on molecular sieve (4 Å). Polyethersulfone (PES) membrane (Φ13 mm × 0.22 µm) was purchased from Jin Teng Experimental Equipment Co., Ltd., Tianjin, China. All the chemical reagents mentioned above were of analytical grade and used without further purification.

2.2. Preparation of metal-organic frameworks

MIL-53(Al) was prepared according to a previously reported procedure [41] briefly, terephthalic acid (1.55 g, 9.36 mmol) was firstly dissolved in DMF (120 mL) in a beaker. Then Al(NO₃)₃·9H₂O (2.36 g, 6.30 mmol) was mixed into terephthalic acid solution. After stirring for 30 min at 25 °C, the solution was transferred into a 200 ml Teflon-lined autoclave and then kept at 220 °C for 72 h. After cooling to 25°C, a white powder was obtained. The sample was washed three times with DMF and anhydrous ethanol, respectively. The collected powder was vacuum dried at 50 °C for 12 h to get final products. After cooling down to room temperature, 1.65 g of MIL-53(Al) had been obtained with the yield of 42.01% and stored in the desiccator with silica gel.

MIL-125(Ti) was prepared by following a previously reported

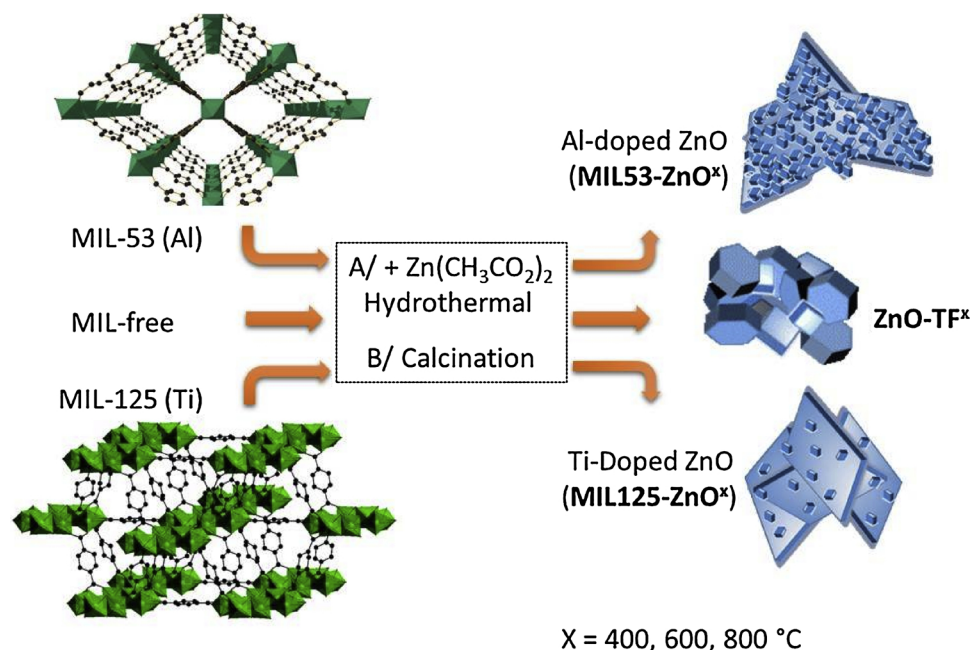


Fig. 1. Nomenclature of the samples and schematic illustration of the fabrication of ZnO nanosheets templated by MIL-125(Ti) and MIL-53(Al).

procedure [42]: terephthalic acid (1.5 g, 9 mmol) was firstly dissolved in a mixture of DMF (27 mL) and methanol (3 mL). Then titanium(IV) n-butoxide (0.78 mL, 2.25 mmol) was mixed with the solution, stirred for 30 min at 25 °C and then introduced into a 100 mL Teflon-lined autoclave, kept at 150 °C for 24 h. After cooling to 25 °C, a white powder was obtained. The sample was washed by DMF and ethanol with three times, respectively. Finally, the powder was vacuum dried at 50 °C for 12 h. After cooling down to room temperature, 0.454 g of MIL-125(Ti) with the yield of 19.91% had been also stored in the desiccator with silica gel.

2.3. Preparation of MIL53-ZnO and MIL125-ZnO using MOFs as reactive templates

ZnO nanocrystals were prepared by hydrothermal method using MIL-53(Al) and MIL-125(Ti) as reactive templates. The detailed procedures were as follows: powder of MIL-53(Al) ($\text{Al(OH)[O}_2\text{C-C}_6\text{H}_4\text{-CO}_2]$) (0.104 g, 0.5 mmol) or MIL-125(Ti) ($\text{Ti}_8\text{O}_8\text{(OH)}_4\text{(O}_2\text{C-C}_6\text{H}_4\text{-CO}_2)_6$) (0.098 g, 0.0625 mmol) was added gradually in a beaker containing an aqueous solution of zinc acetate 0.2 M (40 mL, 8 mmol) with continuously magnetic stirring (400 rpm) for 30 min at 25 °C. Next, under continuous stirring, an aqueous solution of potassium hydroxide 2 M (16 mL, 32 mmol) was added dropwise to the suspension and additionally stirred for 30 min. The mixture is then transferred into a 100 mL Teflon-lined autoclave and reacted at 200 °C for 12 h under static conditions and autogenous pressure. Cooled back to 25 °C in ambient atmosphere, the as-prepared suspension was separated by centrifugation (8000 rpm) for 15 min and washed with anhydrous ethanol (50 mL). Then, the solid product was freeze-dried (-50 °C, vacuum pressure < 10 Pa, 24 h) and the dried product was grinded in the agate mortar to obtain a soft white powder of MIL53-ZnO (0.65 g) and MIL125-ZnO (0.70 g) in respectively 86.8% and 93.6% yield. For comparison, ZnO sample was prepared by the same procedure without addition of any MOFs, it is labelled ZnO-TF.

2.4. Thermal treatment of MIL53-ZnO and MIL125-ZnO

Finally, the powders were calcined at either 400 °C, 600 °C or 800 °C for 2 h (heating rate: 5 °C /min, flow of air) to obtain MIL125-ZnO^x, and MIL53-ZnO^x, with respectively $x = 400, 600$ and 800. ZnO-TF⁴⁰⁰ was obtained by calcination at 400 °C for 2 h of ZnO-TF. After calcination treatment, the yields of the samples were all above 99%.

2.5. Characterizations

The crystal structural properties of samples were analyzed by a (Rigaku, Ultima IV, Japan) X-ray diffractometer (XRD) with Cu K α radiation in the Bragg angle ranging between 5° and 80°. The thermogravimetric analysis (TGA) curves of all the samples were measured using STA-449 thermogravimetric analyzer (Netzsch, Germany) under air atmosphere using a temperature range of 30 °C–800 °C at a heating rate of 10 °C min⁻¹. The surface morphologies of all the samples were measured by (FEI, Nova NanoSEM 230, USA) scanning electron microscopy (SEM) at an accelerating voltage of 5–10 kV, together with (Horiba, XMX 1011, Japan) energy dispersive spectroscopy (EDS). The detailed microstructures of all the samples were investigated by using (JEOL, JEM-2100, Japan) transmission electron microscopy (TEM) with a field emission gun operating at 200 kV. Attenuated Total Reflection Fourier transform infrared (ATR-FTIR) spectra were carried out using an FT-IR spectroscopy (Pekin-Elmer, 1600, USA) within the wavelength range of 400–4000 cm⁻¹. The X-ray photoelectron spectroscopy (XPS) spectra of samples were attained in an ESCALAB 250 instrument (Thermo Scientific, USA) with Al K α radiation monochromatic source. Raman spectra measurements were carried out using Invia Reflex Raman Microscope (Renishaw, UK) equipped with a 532 nm laser source. The specific surface area and pore size distribution of the

samples were both determined by N₂ adsorption /desorption on a Micrometrics ASAP-2010 adsorption apparatus. UV-vis diffuse reflection absorption spectra (UV-vis DRS) were recorded in the range of 300–600 nm by UV-vis spectrophotometer (Shimadzu, UV 3600, Japan) equipped with an integrating sphere using BaSO₄ as a reference. The Photoluminescence spectroscopy (PL) spectra of the samples were investigated using LS55 spectrophotometer (Perkin-Elmer, USA) with 325 nm excitation wavelength. The photocurrent measurements and electrochemical impedance spectroscopy were performed at a VersaSTAT MC electrochemical workstation (Princeton, USA). The measurement was carried out in a conventional three-electrode cell, with a glassy carbon electrode as the working electrode [43], Pt plate and Ag/AgCl electrode as the counter electrode and reference electrode, respectively. Electron paramagnetic resonance (EPR) measurements were performed on an EMXnano spectrometer (Bruker, Germany) operating at a frequency of 9.4 GHz at 77 K. Photo-generated ·OH and ·O₂- radical species in the photocatalytic process were detected with 5,5-Dimethyl-1-pyrroline N-oxide (DMPO) as a trap agent. 50 mg of photocatalyst in the 5 mL of DMPO (0.5 mM) solution was UV-irradiated by a 100 W Hg arc lamp within 5 min.

2.6. Structure models and computational details

First-principles calculations were performed with the projector-augmented wave (PAW) method [44] as implemented in the Vienna ab initio Simulation Package VASP code [45]. The generalized gradient approximation to exchange and correlation of Perdew, Burke and Ernzerhof (PBE) [46] is used for DFT level. Energy cutoff for the plane-wave basis is 500 eV, and a $16 \times 16 \times 10 \text{ \AA}^{-3}$ –centered Monkhorst-Pack k-mesh is used for pristine ZnO calculations. Standard DFT is notorious for its well-known underestimate of bandgap. To obtain reasonable bandgap, we take the DFT + U framework, in which the Dudarev's approach [47] is used for Zn-d states, i.e., $(U-J)_{\text{Zn}} = 6 \text{ eV}$. We also added some non-local external potential (NLEP) parameters for the empirical band-gap correction [48]. The calculated ZnO bandgap is 3.35 eV as shown in Fig. 7, in good agreement with our experimental results 3.22 eV. For ZnO with oxygen vacancies, we construct $3 \times 3 \times 2$ supercell with one oxygen vacancy to obtain impurities concentration comparable with our experiments. Convergence criteria of energy and force are set to $1 \times 10^{-5} \text{ eV}$ and 0.01 eV \AA^{-1} , respectively, for all calculations.

2.7. Evaluation of photocatalytic activity

The photocatalytic performances of the samples were analyzed by the degradation of methyl orange (MO) aqueous solution carried out in a quartz tube reactor under the irradiation of UV source (100 W Hg arc lamp). A suspension of the photocatalyst (25 mg, 0.31 mmol) in an aqueous solution of methyl orange (100 mL, 25 mg/L) was magnetically stirred in the dark at 30 °C for 30 min in order to reach the absorption equilibrium and filtered 5 mL of the suspension with PES membrane. After ignition of the UV source, an aliquot (5 mL of the suspension) was drawn and filtered each using a PES membrane at 15 min, 30 min, 60 min, respectively. The photodegradation efficiency of MO solution was measured by UV-vis spectrophotometer (Shimadzu, UVmini-1240, Japan) under the maximum absorption wavelength (463 nm). Other control experiments, such as pH (controlled by 0.1 M HCl and 0.1 M NaOH), photocatalyst concentration, MO concentration and scavenger (t-Butanol, 5 mL) were carried out according to the above procedure.

3. Results and discussion

ZnO-based materials were prepared as powder and in high yield by a direct one-pot hydrothermal process of Zinc (II) acetate in KOH solution in the presence of powder of either MIL-125(Ti) or MIL-53(Al). These were first characterized in order to identify as much as possible

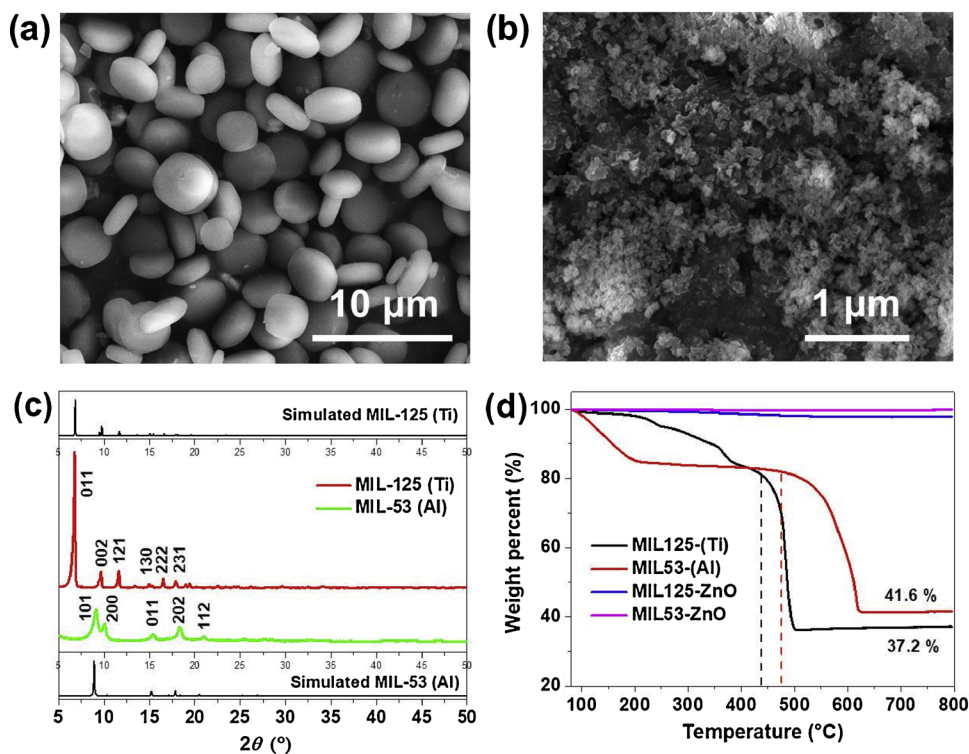


Fig. 2. SEM images of MIL-125(Ti) (a) and MIL-53(Al) (b), XRD patterns of MIL-125(Ti) and MIL-53(Al) (c), TGA curves of MOFs and MIL-ZnO before calcination treatment (d).

their transformation and role during the process of formation of ZnO. The morphologies of the particles of MIL-125(Ti) and MIL-53(Al), a crucial point in the view of their possible effect on the morphology of the resulting ZnO materials. By SEM analysis shown in Fig. 2-a, b, MIL-125(Ti) appeared as micrometric particles (3–5 μm) with morphology in between ovoidal or flat cube with round corners. Differently, the size of the particles of MIL-53(Al) was submicrometric, in the range of 30–100 nm, much smaller than MIL-125(Ti). Nonetheless, from BET analysis in Table S2, both MOFs have very high specific surface area, 776.8 m² g⁻¹ for MIL-53(Al), and up to 984.2 m² g⁻¹ for MIL-125(Ti). However, the pore volume and pore size of MIL-53(Al) were 6.4 times and 4.5 times larger than that of MIL-125(Ti), respectively. MIL-53(Al) and MIL-125(Ti) were both confirmed by X-ray diffraction patterns in Fig. 2-c that were in good accordance with the simulated XRD from cif-files of CCDC 751157 and 220475, respectively. CCDC 751157 and 220475 contain the supplementary crystallographic data for this paper. [49,50] The main peaks of MIL-125(Ti) were assigned to the (011), (002) and (121) planes. [51] And the main bands of MIL-53(Al) were ascribed to the (101), (200), (011), (202) and (112) planes. [52] In the same idea, the FT-IR spectra of MOFs (Figure S1) presented the typical absorbance reported in previous literature for these materials like for MIL-125(Ti) [53] the –COO group (1686 and 1377 cm⁻¹), the –C₄H₆ ring (1018 and 749 cm⁻¹) and the O-Ti-O group at 400–800 cm⁻¹ [54]. The peak at 1273 cm⁻¹ was also assigned to the C–O vibration [55], and the one at 1694 cm⁻¹ to the unreacted free carboxylic groups (–COOH) from terephthalic acid which was also identified by the peak at 1686 cm⁻¹ in the spectrum of MIL-125(Ti) [56].

Hydrothermal treatment of zinc acetate was performed in 2 M KOH solution at 200 °C, with or without MOFs. In the former case the Zn/Ti and Zn/Al molar ratio were equal to 16/1; this low molar ratio being chosen in order to show the effect of a low quantity of MOFs on the synthesis of ZnO. Possible evolution of the MOFs during the hydrothermal treatment is a progressive dissolution leading to soluble species. Although we were not able to identify them, one can propose the formation of organic ones like potassium terephthalate and inorganic

ones like potassium aluminate KAlO₂ or potassium titanate K₄TiO₄. Once separated by centrifugation, the solid ZnO samples were analyzed before or after calcination.

By TGA analysis in air (Fig. 2-d), MIL-125(Ti) and MIL-53(Al) present an inorganic yield or respectively 37.2% and 41.6% at 800 °C corresponding to the formation of respectively TiO₂ and Al₂O₃. For MIL-125(Ti) with the formula of Ti₈O₈(OH)₄(O₂C-C₆H₄–CO₂)₆, [57] the theoretical inorganic yield of TiO₂ should be 40.8% after calcination in air. With formula of Al(OH)[O₂C-C₆H₄–CO₂]₆, ceramic yield for MIL-53(Al) should be 26.0% corresponding to the formation of Al₂O₃ [58]. The discrepancy between the theoretical and experimental values was ascribed of adsorbed water and solvent and this was supported by the important weight loss before 200°C. Aside this, MIL-125(Ti) and MIL-53(Al) were stable up to 436°C and 475°C, respectively. As shown in Fig. 2-d, MIL125-ZnO and MIL53-ZnO present very low weight loss before calcination, respectively 2.1% and 0.3%. After calcination, the weight loss is not significant (Figure S2). It suggests a complete decomposition of the MOFs structure during the hydrothermal process and the removal of any soluble species during the filtration.

Fig. 3-a, b shows the XRD data of ZnO samples prepared by reactive templating with either MIL-53(Al) or MIL-125(Ti) before and after calcination. All diffractograms exhibit the typical diffraction peaks at 31.86°, 34.52°, 36.35°, 47.54°, 56.60°, 62.86°, 66.38°, 67.96° and 69.10° indexed to reflections of ZnO (JCPDS 36–1451; respectively (100), (002), (101), (102), (110), (103), (200), (112) and (201)) and consistent with hexagonal wurtzite structure of ZnO. This is also observed for ZnO-TF⁴⁰⁰ prepared in the absence of any MOFs. Therefore, we assumed that during the hydrothermal treatment, the MOFs structure was completely reacted and destroyed at the same time that the ZnO formed. Careful observation of the spectra did not allow us to identify diffraction peaks of any Ti-containing or Al-containing oxides phases. We further investigated the microstructures of ZnO nanocrystals at different calcination temperatures by measuring the broadness and 2θ peaking of three main crystal planes, namely (100), (002) and (101). In Table S1, the peaks of the three planes had no shifts with different

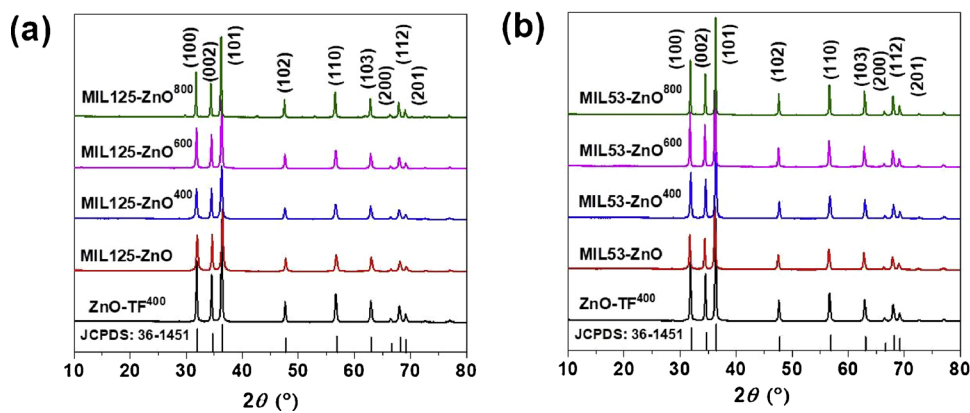


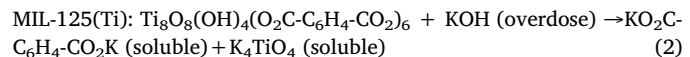
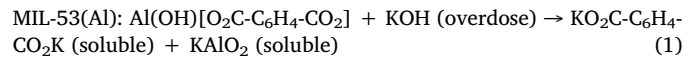
Fig. 3. XRD patterns of ZnO samples using MIL-125(Ti) (a) and MIL-53(Al) (b) as reactive templates.

calcination temperatures either MIL-53(Al) or MIL-125(Ti). However, as expected, the calcination conditions had great influence on the broadness of the signals indicating a grain sizes increase in the following order: $\text{MIL-ZnO}^{400} < \text{MIL-ZnO} \approx \text{ZnO-TF}^{400} < \text{MIL-ZnO}^{600} < \text{MIL-ZnO}^{800}$. More interestingly, using any of the three peaks of the main planes, the crystallites size of ZnO prepared with MIL-125(Ti) was always smaller than that with MIL-53(Al) although, for the starting MOFs themselves, the crystallites size of MIL-53(Al) is much smaller than the one of MIL-125(Ti). N_2 adsorption-desorption isotherms and pore size distribution of all the samples were respectively shown in Figure S3-a, b. BET data, such as the specific surface area, pore size and pore volumes of the samples were listed in Table S2. The specific surface area of MIL-125(Ti) appeared larger than that of MIL-53(Al), but the pore volume and pore size of MIL-125(Ti) were smaller than that of MIL-53(Al). As for the hydrothermal products, the specific surface area of MIL125-ZnO and MIL53-ZnO reached $24.37 \text{ m}^2 \text{ g}^{-1}$ and $15.86 \text{ m}^2 \text{ g}^{-1}$, respectively. Whereas, the pore volume and pore size of MIL125-ZnO were all smaller than MIL53-ZnO, which was similar to the result between MIL-125(Ti) and MIL-53(Al). After the calcination process, all specific surface areas were smaller due the growth and agglomeration of nanograins. The pore volume and pore size of MIL125-ZnO⁴⁰⁰ and MIL53-ZnO⁴⁰⁰ were a little bigger than for the non-calcined ones, suggesting a collapse of porous structure, resulting in larger mesopores.

From SEM analysis in Fig. 4, showed the morphologies of ZnO-TF, MIL125-ZnO and MIL53-ZnO notably differences between each other. This is a clear evidence of the effect of the MOFs. These differences are not lost upon calcination up to 400 °C. And for instance, the pure ZnO of ZnO-TF before or after calcination, exhibits the six square prism structure with about 200 nm section diameter and 350 nm in length. Differently, MIL125-ZnO⁴⁰⁰ presented a nanoplate or flaky morphology with a little amount of ultrafine nanosheets of which the thickness was 50 nm. Compared to the MIL125-ZnO⁴⁰⁰, MIL53-ZnO⁴⁰⁰ exhibits this flaky morphology but with much more ultrafine nanosheets in the samples. On the one hand, increase of temperature of calcination led to an increase of the ZnO nanoplates' size derived from MIL-125(Ti) and MIL-53(Al), and on the other hand, the thickness of ZnO nanoplates templated by MIL-125(Ti) gradually changed from 30 nm to 80 nm, and the thickness of MIL53-ZnO^x grew from 40 nm to 90 nm. As for the ultrafine nanosheets of MIL-ZnO, MIL125-ZnO^x extended from about the size of 50 nm to 100 nm with the increase of calcination temperature, while MIL53-ZnO^x notably enlarged from 50 nm to 200 nm. From energy dispersive spectroscopy in Fig. 4-k, l, MIL125-ZnO and MIL53-ZnO were mainly composed of zinc and oxygen with low amount of Ti and Al, respectively. Therefore, it was the first indication that Ti and Al from MIL-125(Ti) and MIL-53(Al) were integrated into the MOF-templated ZnO samples. The high-resolution TEM (HRTEM) (Fig. 5-a-f) of regions showed the characteristic lattices fringes of 0.281 nm, 0.265 nm

and 0.272 nm, which were assigned to the (101) plane of ZnO-TF⁴⁰⁰, MIL125-ZnO⁴⁰⁰ and MIL53-ZnO⁴⁰⁰, respectively. Compared to the ZnO-TF⁴⁰⁰, the lattices fringes of the MIL125-ZnO⁴⁰⁰ and MIL53-ZnO⁴⁰⁰ was narrowed, and could result from the crystallites size that was reduced in those cases according to the data of Table S1. Furthermore, the SAED patterns in Fig. 5-g and h indicated that the MIL125-ZnO⁴⁰⁰ and MIL53-ZnO⁴⁰⁰ were polycrystalline materials containing (100), (002), (101), (102), (110) and (103), as also found by XRD (Fig. 3-a, b). Fig. 5-i and j shows the EDS maps of MIL125-ZnO⁴⁰⁰ and MIL53-ZnO⁴⁰⁰, which re-confirms the presence of Zn, O, Ti and Al, this being an additional indication of Ti and Al incorporation thereof initially present in the MOFs.

It is known that the morphology of ZnO can be controlled at the nanoscale by the use of directing agent [59], or by playing with the pH and Zn(II) concentration in hydrothermal process [60]. In the present case, dissolution of MIL-53(Al) and MIL-125(Ti) gives soluble salts due to overdose of alkali source can react with ligands and metal ions as following functions:



This process may contain competitive mechanism. Due to the OH^- ions were overdose, Al^{3+} and Ti^{4+} from MOFs not only transformed into soluble salts (mainly), but also doped in ZnO nanocrystals growing (minor). At the same time, the terephthalate anion released in the solution by the MOFs can be considered as one of the possible explanation for the lamellar morphology of ZnO here. The kinetics of dissolution of the MOFs were different for MIL-53 and MIL-125 and probably also the amount of dissolved cations and anions. However, it has also been shown that metal cations can also lead to an orientation of the morphology of ZnO nanoparticles, especially in the case of Al(III) [61]. Since Al (III), Ti (VI) is hexacoordinated, a similar effect on crystal growth of ZnO can be expected.

Additional characterization was made by XPS reported in Fig. 6 that shows the spectra of ZnO samples after calcinations at 400°C. From the full-pattern spectra of Fig. 6-a, it can be seen that beside Zn and O the presence of either Ti or Al is clearly related to the use of respectively MIL-125(Ti) or MIL-53(Al). The presence of carbon (284.8 eV) with low intensity was ascribed to the carbon dioxide adsorbed on the samples [62]. In Fig. 6-b, for ZnO-TF⁴⁰⁰, the peaks at 1044.5 eV and 1021.4 eV were ascribed as Zn 2p_{1/2} and Zn 2p_{3/2} levels of Zn^{2+} in ZnO [63], in which the gap of binding energy was 23.1 eV. For MIL125-ZnO⁴⁰⁰ and MIL53-ZnO⁴⁰⁰, the binding energies of Zn 2p_{1/2} and Zn 2p_{3/2} was very little negatively shifted, possibly due to electronic effect or different valence states with Zn^{2+} . Concomitantly, the gap of binding energies between Zn 2p_{1/2} and Zn 2p_{3/2} of MIL125-ZnO⁴⁰⁰ or MIL53-ZnO⁴⁰⁰ all

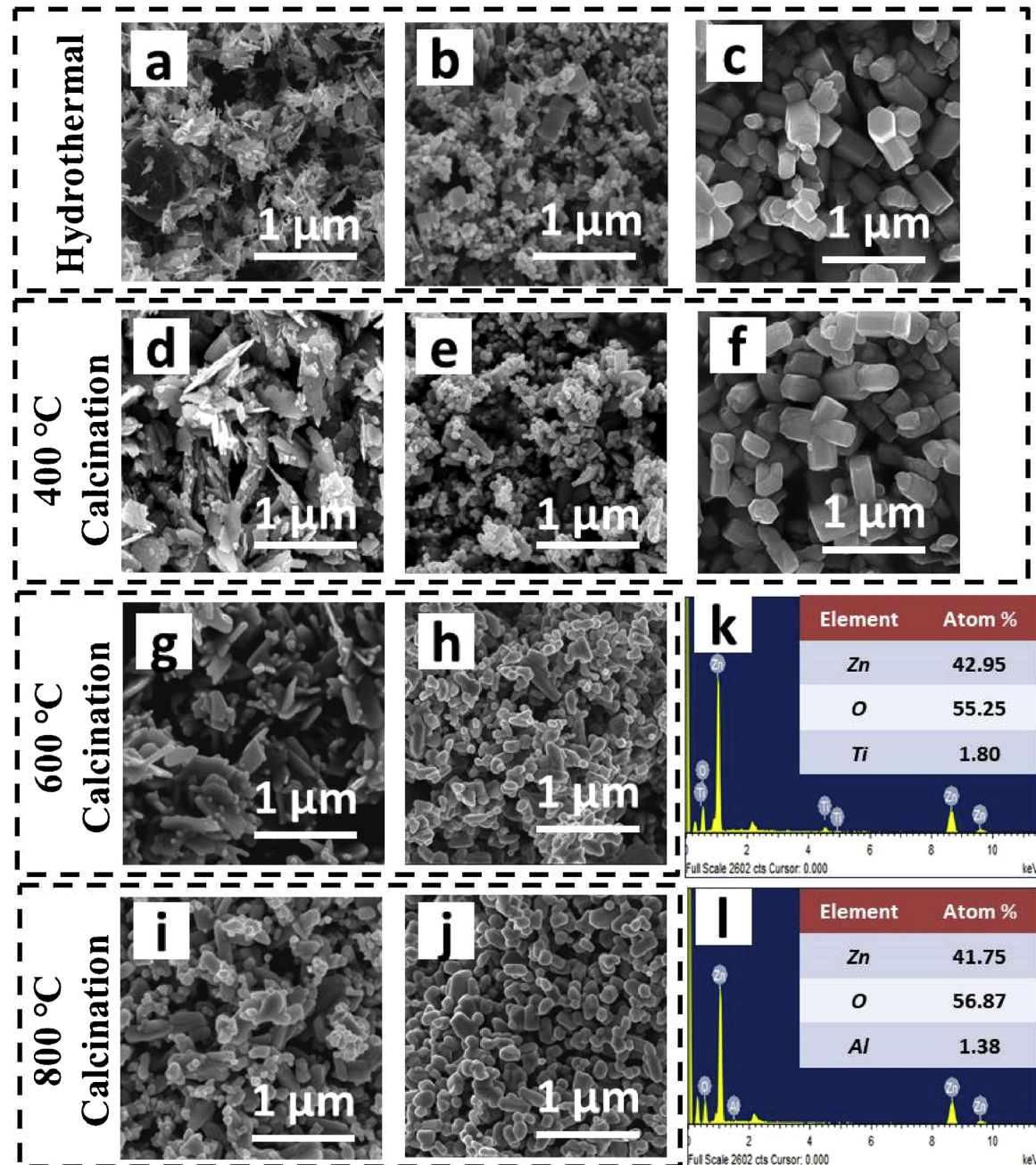


Fig. 4. SEM images of MIL125-ZnO (a), MIL53-ZnO (b), ZnO-TF (c), MIL125-ZnO⁴⁰⁰ (d), MIL53-ZnO⁴⁰⁰ (e), ZnO-TF⁴⁰⁰ (f), MIL125-ZnO⁶⁰⁰ (g), MIL53-ZnO⁶⁰⁰ (h), MIL125-ZnO⁸⁰⁰ (i), MIL53-ZnO⁸⁰⁰ (j); EDS of MIL125-ZnO⁴⁰⁰ (k), MIL53-ZnO⁴⁰⁰ (l).

retain at 23.1 eV, which are in accordance with the sample of ZnO-TF⁴⁰⁰. From O 1 s XPS spectra in Fig. 6-c, deconvolution by Gaussian distribution suggests three peaks centered at 530.0 eV, 531.6 eV and 533.3 eV, and presently attributed to respectively the lattice oxygen O_I, vacancy oxygen O_{II} and O_{III} the loosely bound oxygen adsorbed onto the surface of ZnO [64]. Their relative proportions in Table 1 reveal that the presence of the MOF and its nature has some influence. It is not understood at present but could be related to the presence of Ti and Al introduced into the ZnO and possibly decrease the percentage of lattice oxygen of ZnO, but increase the content of vacancy oxygen [65]. The relative peak area of vacancy oxygen of MIL125-ZnO⁴⁰⁰ and MIL53-ZnO⁴⁰⁰ is respectively 1.3 and 1.8 times that of ZnO-TF⁴⁰⁰, indicating that more oxygen defects have been generated by the presence of MIL125-(Ti) and MIL53-(Al). As shown in Fig. 6-d, the binding energies of Ti 2p_{3/2} and Ti 2p_{1/2} are located at 458.4 eV and 463.9 eV,

respectively, which are identical to that of Ti⁴⁺ of TiO₂ [66]. In the case of Al 2p_{3/2}, the binding energy peak at 73.9 eV can be attributed to the presence of Al³⁺ of Al₂O₃ [67]. Obviously, due to the electronic interaction between embedded Ti⁴⁺, Al³⁺ and Zn²⁺, the Ti-O-Zn and Al-O-Zn bindings were formed in the MIL125-ZnO⁴⁰⁰ and MIL53-ZnO⁴⁰⁰ lattices, respectively. That resulted in a slight lowering binding energies of Ti⁴⁺ and Al³⁺ compared to the reported references [68,69]. These results once more confirm that Ti and Al had been ideally doped into ZnO lattices.

To get insight into the effect of the intrinsic structural oxygen vacancy on the photocatalytic activities, DFT computations were performed. The bandgap structures and electronic density of states (DOS) of both pure ZnO and oxygen-defective ZnO were investigated and the results were illustrated in Fig. 7. The valence band (VB) of ZnO is mainly attributable to the O-orbit below Fermi level and the conduction

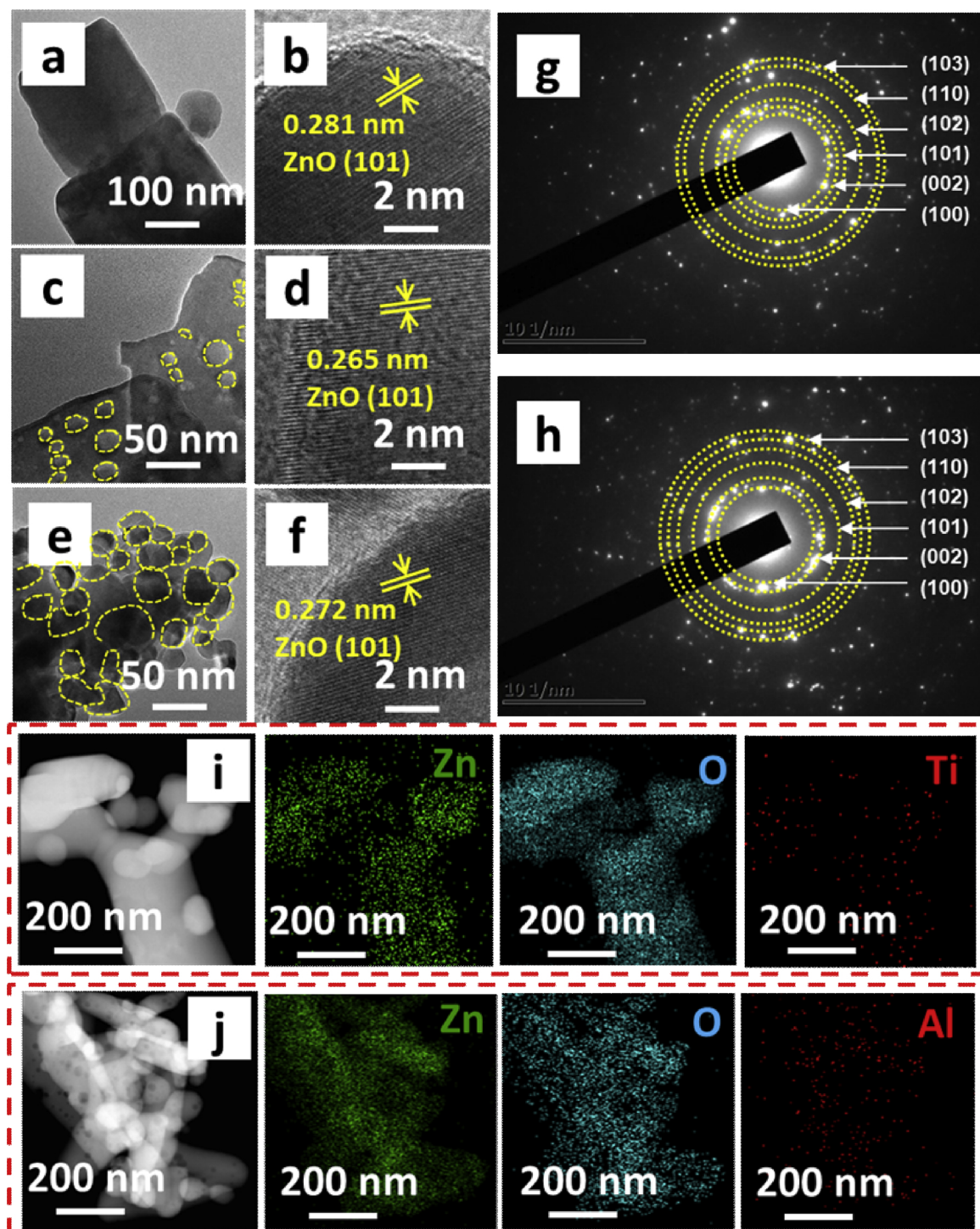


Fig. 5. TEM images of ZnO-TF⁴⁰⁰ (a), (b), MIL125-ZnO⁴⁰⁰ (c), (d), MIL53-ZnO⁴⁰⁰ (e), (f); SAED images of MIL125-ZnO⁴⁰⁰ (g), MIL53-ZnO⁴⁰⁰ (h); EDS mapping images of MIL125-ZnO⁴⁰⁰ (i), MIL53-ZnO⁴⁰⁰ (j).

band (CB) is assigned to the Zn-orbit above Fermi level. Upon involving with oxygen vacancy, the bandgap of ZnO was greatly reduced from 3.35 eV to 2.49 eV, and it should be noted that this bandgap might be underestimated because of the derivative discontinuity of the exchange-correlation function in DFT computation. Importantly, examination of the VB width of oxygen-defective ZnO indicates a slightly increase in comparison with that of pure ZnO, which is suggestive of a significantly enhanced holes mobility and an effectively strengthened oxidation activity of the holes. And similarly, the blue shifted and broadened CB also manifests the higher mobility of electrons [70]. Undoubtedly,

involving oxygen vacancies is able to narrow the band gap of ZnO by generating new valence band and further extend its light absorption which improved the photocatalytic activity [71]. Therefore, the existence of oxygen vacancies in ZnO fulfilling narrow the band gap and promote the motilities and activities of the photo-induced electron-hole pairs, which will be confirmed by the optical and photocatalytic performance as shown below.

In view of their photocatalytic activity, UV-DRS detecting was obtained for ZnO samples after calcinations at 400°C to further investigate the adsorbed wavenumbers and band gap. The latter was calculated by

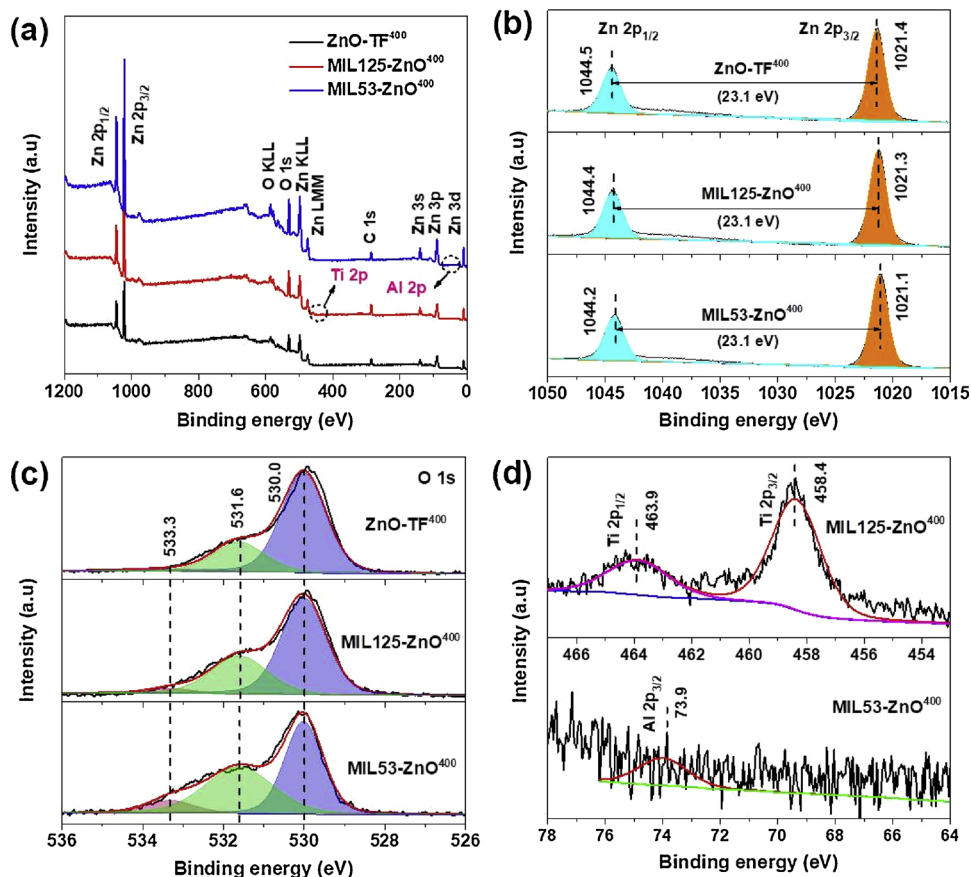


Fig. 6. XPS spectra of ZnO samples (a), the spectra of Zn 2p peak of ZnO samples (b), the spectra of O 1s peak of ZnO samples (c), the spectra of Ti 2p and Al 2p peaks of ZnO samples (d).

Table 1
The amount of O_{1s} in the ZnO samples.

Samples	E _O /eV (A _O /A _{total} %)		
	Lattice O _I	Vacancy O _{II}	Adsorbed O _{III}
ZnO-TF ⁴⁰⁰	530.0 (72.6)	531.6 (24.4)	533.3 (3.0)
MIL125-ZnO ⁴⁰⁰	530.0 (65.1)	531.6 (32.1)	533.3 (2.8)
MIL53-ZnO ⁴⁰⁰	530.0 (48.2)	531.6 (43.8)	533.3 (8.0)

$E_g = 1240 / \lambda$ as abscissa and $(\alpha h\nu)^2$ as ordinate in Fig. 8-a [72]. The band gap was obtained from the intersection of tangent along the upper part of the curves and abscissa. From Fig. 8-a, the band gap of ZnO-TF⁴⁰⁰, MIL125-ZnO⁴⁰⁰ and MIL53-ZnO⁴⁰⁰ was 3.22 eV, 3.21 eV and 3.18 eV, respectively. Thus, the absorption edge of MIL53-ZnO⁴⁰⁰ was 390 nm, a slightly higher value compared to the one for MIL125-ZnO⁴⁰⁰ (386 nm) and ZnO-TF⁴⁰⁰ (385 nm). It evidences the possible effects of the integration of the MOF-derived cation and oxygen defects in the ZnO crystals, reducing the band gap of ZnO and consequently to a possible absorption of a higher proportion of the incident light. To better investigate the band structure of ZnO samples, valence band (VB) positions of ZnO-TF⁴⁰⁰, MIL125-ZnO⁴⁰⁰ and MIL53-ZnO⁴⁰⁰ were further tested by XPS spectra and calculated through linear extrapolation method [73]. In Figure S4, the VB values of ZnO-TF⁴⁰⁰, MIL125-ZnO⁴⁰⁰ and MIL53-ZnO⁴⁰⁰ were respectively 2.78 eV, 2.59 eV and 2.35 eV. Thus, the conductive band (CB) positions of ZnO-TF⁴⁰⁰, MIL125-ZnO⁴⁰⁰ and MIL53-ZnO⁴⁰⁰ were -0.44 eV, -0.62 eV and -0.83 eV, respectively, according to the band gaps and VB values.

Raman spectroscopy is a very effective technique for investigating the microstructure and crystal defects sometime not detected by XRD. In Fig. 8-b, the Raman spectra of ZnO-TF⁴⁰⁰, MIL125-ZnO⁴⁰⁰ and

MIL53-ZnO⁴⁰⁰ all show three predominant Raman modes centered at 330 cm^{-1} , 380 cm^{-1} and 437 cm^{-1} assigned to E_{2H} - E_{2L} , A_1^{LO} and E_{2H} phonon modes, respectively. The signal at 437 cm^{-1} is the most intense peak in all the samples and correspond to the Wurtzite hexagonal structure of ZnO. [74] The lower intensity of E_{2H} in the MIL125-ZnO⁴⁰⁰ and MIL53-ZnO⁴⁰⁰ compared to the one of ZnO-TF⁴⁰⁰ can be ascribed to lower crystallites sizes [75] observed by XRD, which was verified that grain size of three main facets of MIL125-ZnO⁴⁰⁰ and MIL53-ZnO⁴⁰⁰ was smaller than that of ZnO-TF⁴⁰⁰ in Table S1. Importantly, the Raman peak at 575 cm^{-1} of ZnO-TF⁴⁰⁰ belonged to E_1^{LO} mode, which can be assigned to the contribution of oxygen vacancies. Due to Ti and Al doping in the ZnO, E_1^{LO} peak at 575 cm^{-1} had red shifted and broadened to 584 cm^{-1} and 586 cm^{-1} in the Raman peaks of MIL53-ZnO⁴⁰⁰ and MIL125-ZnO⁴⁰⁰, respectively. This red shift and broadening can suggest the increase of defects such as oxygen vacancies [76].

PL measurements were investigated for optical properties of the ZnO-TF⁴⁰⁰, MIL125-ZnO⁴⁰⁰ and MIL53-ZnO⁴⁰⁰ with 325 nm excitation wavelength as shown in Fig. 8-c. The synthesized ZnO-TF⁴⁰⁰ shows an emission at 382 nm that referred as UV band edge emission (UV emission) which originates from recombination of the free excitons [77]. Besides, the emission peak at 675 nm (defect emission) in the PL curve of ZnO-TF⁴⁰⁰ can be assigned to the intrinsic oxygen defects that are attributed to the recombination of photo-generated holes [78]. The peak at 675 nm for MIL125-ZnO⁴⁰⁰ and MIL53-ZnO⁴⁰⁰ is clearly more intense than for ZnO-TF⁴⁰⁰, while the intensity of the peak at 382 nm had no changes. To estimate the photocatalytic activity, the ratio between defect peak and UV emission peak is sometimes used, in the present case, this ratio is $\text{MIL53-ZnO}^{400} > \text{MIL125-ZnO}^{400} > \text{ZnO-TF}^{400}$. This is in agreement with proportion of oxygen vacancies determined by XPS above in the MIL-125(Ti) and MIL-53(Al). In Fig. 8-d, with Al and Ti doped into ZnO nanocrystals, the MIL125-ZnO⁴⁰⁰ and

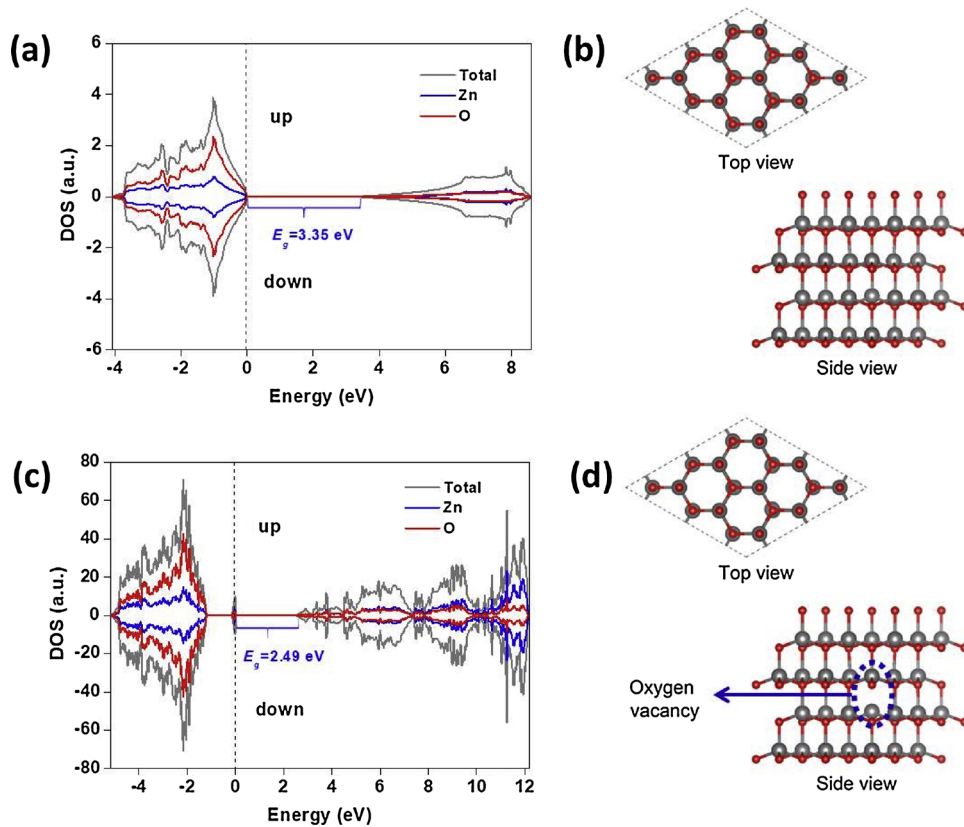


Fig. 7. Total density of states (DOS) of perfect ZnO (a) and oxygen-defective ZnO (c), optimized surface configuration of perfect ZnO (b) and oxygen-defective ZnO (d). The dotted lines at energy zero represent the Fermi level.

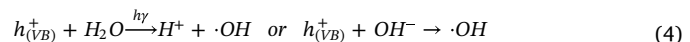
MIL53-ZnO⁴⁰⁰ presented higher photocurrent than that of ZnO-TF⁴⁰⁰, suggesting that the separation of photogenerated charge carriers is greatly promoted. Also, Nyquist impedance plots of ZnO-TF⁴⁰⁰, MIL125-ZnO⁴⁰⁰ and MIL53-ZnO⁴⁰⁰ were displayed in Fig. 8-e. MIL125-ZnO⁴⁰⁰ and MIL53-ZnO⁴⁰⁰ exhibited smaller slope than ZnO-TF⁴⁰⁰, suggesting that MIL125-ZnO⁴⁰⁰ and MIL53-ZnO⁴⁰⁰ will meet less resistance under light.

The defects over the ZnO-TF⁴⁰⁰, MIL125-ZnO⁴⁰⁰ and MIL53-ZnO⁴⁰⁰ were characterized by EPR testing. As shown in Fig. 8-f, the field signal at $g = 1.96$ can be attributed to the defects related to oxygen vacancies [79,80]. Notably, MIL53-ZnO⁴⁰⁰ displayed stronger signals than that of MIL125-ZnO⁴⁰⁰ and ZnO-TF⁴⁰⁰, indicating the order of V_o content: MIL53-ZnO⁴⁰⁰ > MIL125-ZnO⁴⁰⁰ > ZnO-TF⁴⁰⁰. Thus, with the increase of oxygen defects in the ZnO samples, more oxidative holes will be photo-generated, which are favor to photocatalytic performance [81].

The photocatalytic activity of ZnO samples prepared with or without MOFs templates was tested by photodegradation of methyl orange (MO) under UV-irradiation at 25°C with the initial pH 7. Other control experiments, such as pH, photocatalyst concentration, methyl orange concentration and scavenger (*t*-Butanol) have been optimized in Figure S5. In Fig. 9-a-d and Table S3, photodegradation of MO is plotted as a function of $(C_0 - C_t) / C_0 \times 100\%$, with $C_0 = [\text{MO}]$ after equilibration in the dark, $C_t = [\text{MO}]$ under UV-irradiation at different time. From Fig. 9-a and b, methyl orange had been removed by 98.15% and 96.89% after 60 min of irradiation, respectively using MIL53-ZnO⁴⁰⁰ and MIL125-ZnO⁴⁰⁰. These non-optimized data corresponded to a significant improvement of the photocatalytic activity (+15%) when compared to the 83.10% removal by ZnO-TF⁴⁰⁰. The data from Table S3 not only shows a higher removal of MO using ZnO prepared by reactive templating with MOFs, but also a higher rate constant of MO degradation. Fig. 9-c and d shows that photocatalytic rate of ZnO-TF⁴⁰⁰ was only $2.97 \times 10^{-2} \text{ min}^{-1}$, by comparison the rate constants are the

highest for MIL53-ZnO⁴⁰⁰ and MIL125-ZnO⁴⁰⁰, respectively with 2.24 times and 1.94 times the one for ZnO-TF⁴⁰⁰. Compared with data of the literature reported in Table 2, the ultrafine MIL53-ZnO⁴⁰⁰ nanosheets appear among the highest active materials. Figure S6-a-c show full wavelength curves for photocatalytic degradation of methyl orange (MO) at different reaction times of ZnO-TF⁴⁰⁰, MIL125-ZnO⁴⁰⁰ and MIL53-ZnO⁴⁰⁰, respectively. The photodegradation rates of MIL125-ZnO⁴⁰⁰ and MIL53-ZnO⁴⁰⁰ for MO appear both faster than ZnO-TF⁴⁰⁰. The maximum absorption peak at 463 nm for MO molecule became smaller with the reaction time, which was due to the removal of MO molecule. Besides, the maximum absorption peak at 463 nm for MO had been shifting to shorter wavelength because MO had been degraded into other small molecules [83]. Photostability of ZnO-TF⁴⁰⁰, MIL53-ZnO⁴⁰⁰ and MIL125-ZnO⁴⁰⁰ were investigated by reusing these catalysts in consecutive methyl orange (MO) degradation reactions under UV-irradiation. The photocatalyst was washed with deionized water three times and vacuum dried at 60 °C for six hours. Figure S6-d shows that all the samples exhibit a great durability and there are no significant changes in the photocatalytic activity after five cycles.

In order to investigate the mechanism of photocatalytic reaction, EPR spectra of ZnO-TF⁴⁰⁰, MIL125-ZnO⁴⁰⁰ and MIL53-ZnO⁴⁰⁰ suspensions under UV irradiation were measured to detect the formation of generated radical species using DMPO as capture agent. It is well known that photo-induced holes and electrons are of great importance to implement the photocatalytic process: [86,87]



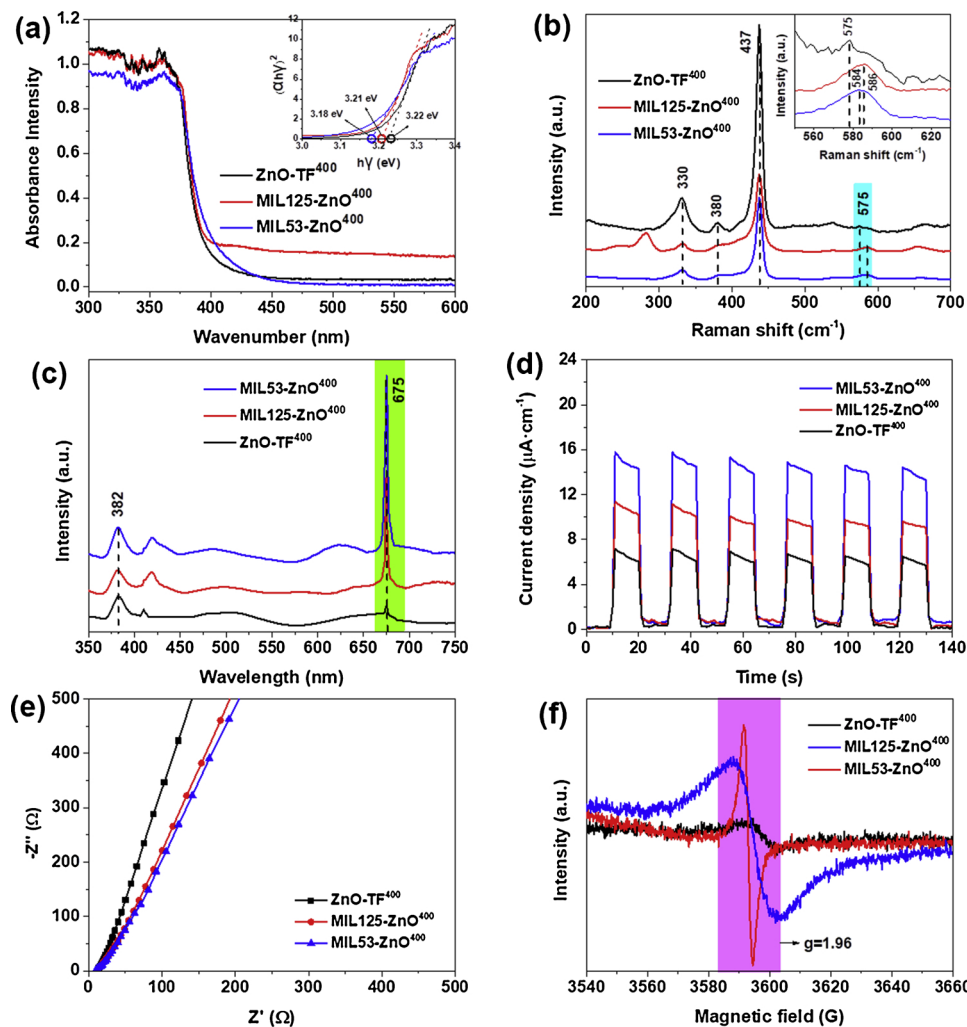


Fig. 8. Characterization of ZnO-TF⁴⁰⁰, MIL125-ZnO⁴⁰⁰ and MIL53-ZnO⁴⁰⁰ by UV-vis DRS and UV-vis relationship between band gap energy and $(\alpha h\nu)^2$ (a), Raman spectra (b), PL spectra (c), Photocurrent response (d), Nyquist impedance plots (e), EPR spectra (f).



As shown in Fig. 9-e,f, after 5 min UV irradiation, the emerging peaks were ascribed to trapped hydroxyl radicals ($\cdot OH$) and superoxide radical anions ($\cdot O_2^-$). While, neither of the signals of $\cdot OH$ and $\cdot O_2^-$ was detected under dark condition. Under UV irradiation, signals of either $\cdot OH$ or $\cdot O_2^-$ were clearly observed, which is generally due to two phenomena: photo-induced holes in the valence band (VB) can react with H_2O or OH^- to generate $\cdot OH$ while electrons in the conduction band (CB) can reduce oxygen molecules into $\cdot O_2^-$. In addition, the signals of $\cdot OH$ were stronger than $\cdot O_2^-$ that indicated that $\cdot OH$ generated from $h_{(VB)}^+$ played the main role while the $\cdot O_2^-$ produced from $e_{(CB)}^-$ played the minor role in the photodegradation of MO. Under UV irradiation, electrons are excited from VB to CB in ZnO, leaving holes on the VB. Therefore, the holes and electrons are separated in ZnO. Thus, $\cdot OH$ and $\cdot O_2^-$ are respectively generated by holes and electrons. Compared to the ZnO-TF⁴⁰⁰, the signals of $\cdot OH$ and $\cdot O_2^-$ belonged to the MIL125-ZnO⁴⁰⁰ and MIL53-ZnO⁴⁰⁰ were more intense, which indicated that ZnO rich in oxygen defects could produce more oxidative holes.

To propose an explanation of the high activity and the higher rate

constant for MIL53-ZnO⁴⁰⁰ than that of MIL125-ZnO⁴⁰⁰, we first note that the MOFs reactive templating processing of ZnO easily introduces abundant oxygen defects into ZnO crystals and affects the band gap, the one of MIL53-ZnO⁴⁰⁰ being slightly narrower than the MIL125-ZnO⁴⁰⁰. On the one hand, oxygen defects in the ZnO crystal are not only as trap center, but also create impurity layer near valence band which produces more holes in the VB layer, besides, causes band gap narrowing and incident light absorption increasing. On the other hand, MOFs reactive templating also impact porosity, indeed the specific surface area of MIL53-ZnO⁴⁰⁰ is smaller than the one of MIL125-ZnO⁴⁰⁰, but the pore volume of MIL53-ZnO⁴⁰⁰ is larger than the MIL125-ZnO⁴⁰⁰ and might be suitable for the formation and diffusion of reactive species at the surface of the photocatalyst. Finally, the MOFs reactive templating by MIL-125(Ti) and MIL-53(Al) produce a different morphology in each case, a point that may favor more active sites of the ZnO nanocrystals as illustrated in Fig. 10.

4. Conclusions

The preparation of ZnO nanocrystals in the presence of Zn-free MOFs is a new approach of the use of MOFs in metal oxide processing. In the case of ZnO prepared by hydrothermal process, Zn-free MOFs have major impact on their characteristics. MIL-125(Ti) and MIL-53(Al) act as a reactive template affecting differently the morphology, the structure and the properties of the resulting ultrafine nanosheets ZnO.

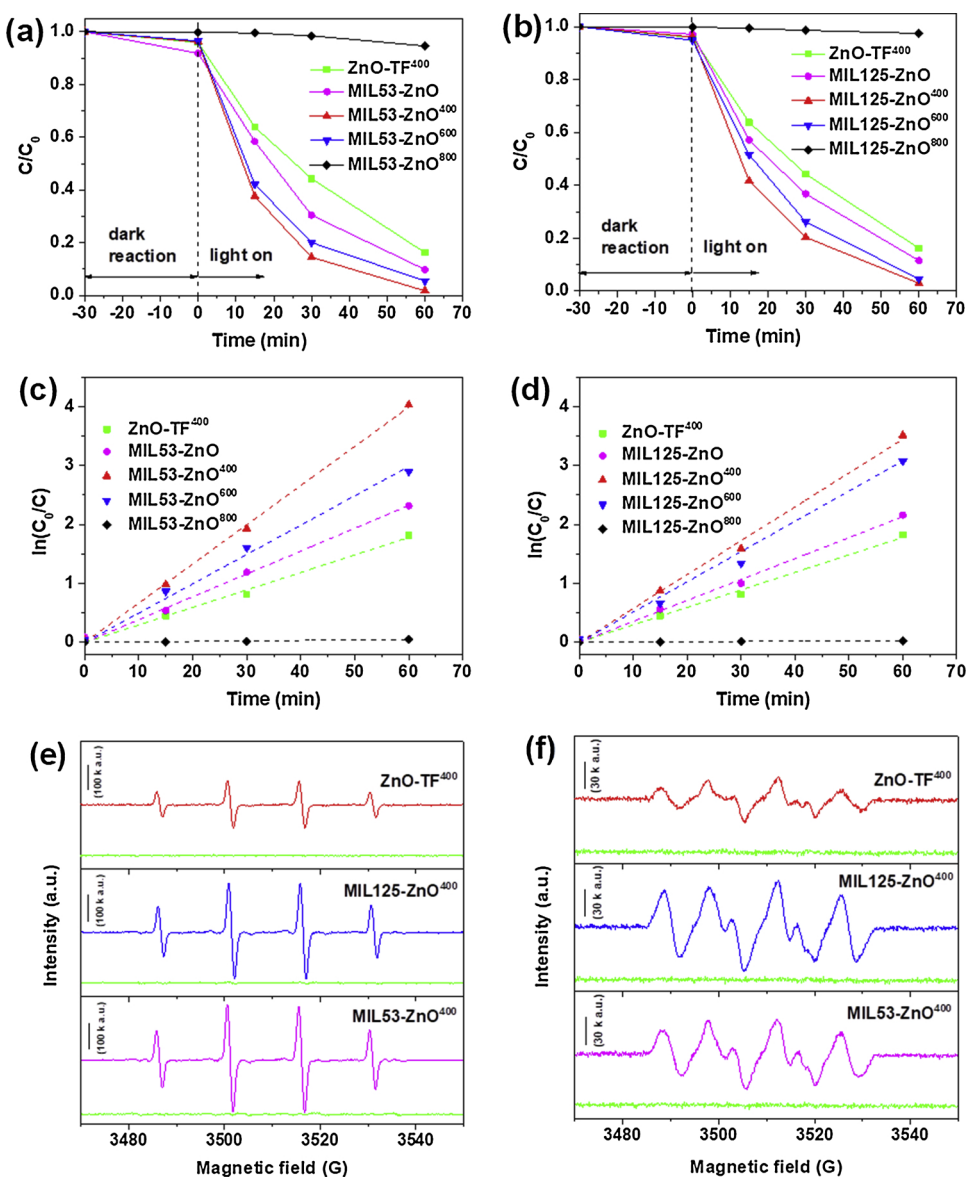


Fig. 9. Photocatalytic degradation curves of methyl orange on ZnO using MIL-53(Al) (a), (c) and MIL-125(Ti) (b), (d) as reactive templates, EPR spectra of DMPO-·OH radicals species (e) and DMPO-·O₂[·] radicals species (f), color solid lines for the radicals species after 5 min UV irradiation, all the green solid lines for the radicals species under dark condition (For interpretation of the references to colour in this figure legend, the reader is referred to the web version of this article).

Table 2

Comparison of photocatalytic activity of MOF-derived ZnO nanomaterials with other recently reported ZnO photocatalysts.

N.	Morphology	Catalyst Conc. (g/L)	MO conc. (mg/L)	UV- irradiation (min)	Degradation (%)	k_{app} (min ⁻¹) $\times 10^{-2}$	Ref.
1	Spindle	0.6	20	180	95	1.04	[82]
2	Nanorod	4	20	120	95	3.35	[69]
3	Spherical	1	9.8	80	complete	5.73	[83]
4	Corn seed	0.5	10	90	99.7	5.99	[84]
5	Nanosheet	1.5	16.4	240	98	1.35	[85]
6	MIL53-ZnO ⁴⁰⁰	0.25	25	60	98.15	6.65	Present work

Compared to ZnO prepared in MOF-free conditions, the improved photocatalytic activity is ascribed to the morphology, specific surface area, Ti or Al content (< 2%) and also to abundant oxygen defects

associated with the presence of the Zn-free MOFs at the synthesis stage. Altogether, this is opening a new route of broad scope for the preparation of metal oxide by using MOFs in a new role.

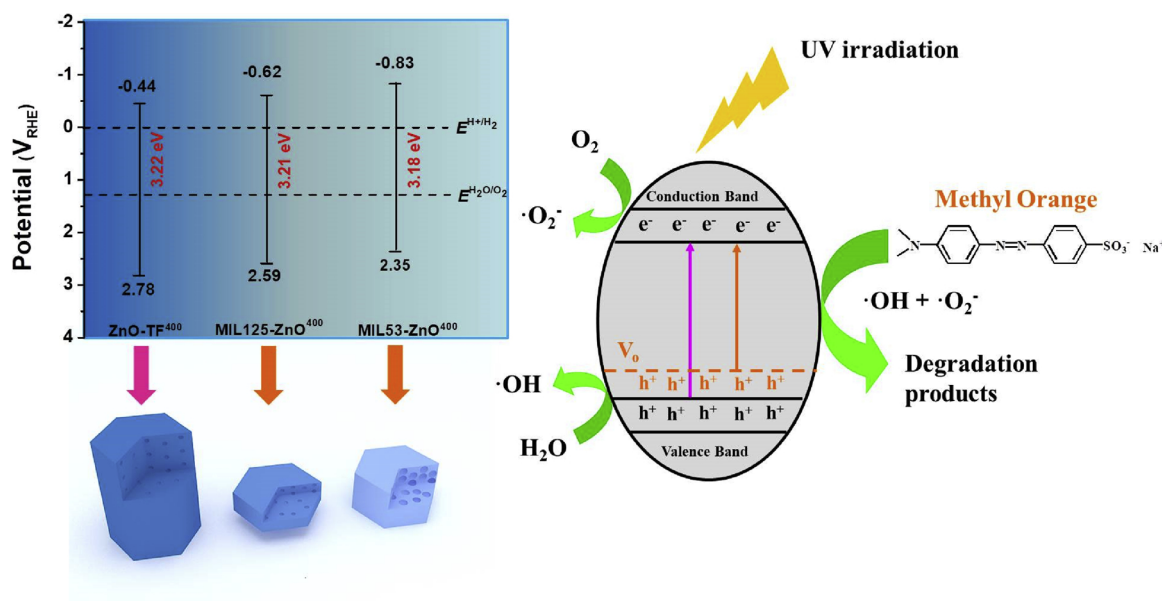


Fig. 10. Illustration for the photocatalytic degradation of MO over traditional ZnO nanorods and defect-rich ZnO nanosheets (V_o is oxygen vacancies).

Acknowledgments

This work was supported by the National Key Research and Development Program of China (2017YFD601005), Natural Science Foundation of China (31700519), Natural Science Foundation of Fujian (2018J01591), Science Fund of Fujian Provincial University (JK2017013).

Appendix A. Supplementary data

Supplementary material related to this article can be found, in the online version, at doi:<https://doi.org/10.1016/j.apcatb.2018.11.026>.

References

- [1] F. Ye, F. Wang, C.C. Meng, L.J. Bai, J.Y. Li, P.X. Xing, B.T. Teng, L.H. Zhao, S. Bai, *Appl. Catal. B-Environ.* 230 (2018) 145–153.
- [2] L.I. Granone, F. Sieland, N. Zheng, R. Dillert, D.W. Bahnemann, *Green Chem.* 20 (2018) 1169–1192.
- [3] W. Yu, J. Zhang, T. Peng, *Appl. Catal. B-Environ.* 181 (2016) 220–227.
- [4] A. McLaren, T. Valdes-Solis, G. Li, S.C. Tsang, *J. Am. Chem. Soc.* 131 (2009) 12540–12541.
- [5] K.M. Lee, C.W. Lai, K.S. Ngai, J.C. Juan, *Water Res.* 88 (2016) 428–448.
- [6] J. Jean, S. Chang, P.R. Brown, J.J. Cheng, P.H. Rekemeyer, M.G. Bawendi, S. Gradecak, V. Bulovic, *Adv. Mater.* 25 (2013) 2790–2796.
- [7] A. Kim, Y. Won, K. Woo, C.-H. Kim, J. Moon, *ACS Nano* 7 (2013) 1081–1091.
- [8] L. Wang, Y. Kang, X. Liu, S. Zhang, W. Huang, S. Wang, *Sens. Actuator B-Chem.* 162 (2012) 237–243.
- [9] X. Liu, J. Zhang, L. Wang, T. Yang, X. Guo, S. Wu, S. Wang, *J. Mater. Chem.* 21 (2011) 349–356.
- [10] K. Qi, B. Cheng, J. Yu, W. Ho, *J. Alloys. Compd.* 727 (2017) 792–820.
- [11] X. Gu, C. Li, S. Yuan, M. Ma, Y. Qiang, J. Zhu, *Nanotechnology* 27 (2016) 1–21.
- [12] Q. Han, J. Pang, X. Wang, X. Wu, J. Zhu, *Chem. Eur. J.* 23 (2017) 3891–3897.
- [13] F. Xiong, L.-L. Yin, Z. Wang, Y. Jin, G. Sun, X.-Q. Gong, W. Huang, *J. Phys. Chem. C* 121 (2017) 9991–9999.
- [14] M. Wang, X. Cao, L. Wang, L. Zhang, *J. Porous. Mat.* 17 (2010) 79–84.
- [15] F.-H. Ko, W.-J. Lo, Y.-C. Chang, J.-Y. Guo, C.-M. Chen, *J. Alloys Compd.* 678 (2016) 137–146.
- [16] J. Liu, Y. Zhao, J. Ma, Y. Dai, J. Li, J. Zhang, *Ceram. Int.* 42 (2016) 15968–15974.
- [17] L.-J. Chen, Y.-J. Chuang, *Mater. Lett.* 68 (2012) 460–462.
- [18] Y. Liu, J.F. Eubank, A.J. Cairns, J. Eckert, V.C. Kravtsov, R. Luebke, M. Eddaaoudi, *Angew. Chem. Int. Ed.* 46 (2007) 3278–3283.
- [19] P. Li, N.A. Vermeulen, X. Gong, C.D. Malliakas, J.F. Stoddart, J.T. Hupp, O.K. Farha, *Angew. Chem. Int. Ed.* 55 (2016) 10358–10362.
- [20] D. Saha, Z. Bao, F. Jia, S. Deng, *Environ. Sci. Technol.* 44 (2010) 1820–1826.
- [21] S.S. Kaye, A. Dailly, O.M. Yaghi, J.R. Long, *J. Am. Chem. Soc.* 129 (2007) 14176–14177.
- [22] I.A. Khan, Y. Qian, A. Badshah, M.A. Nadeem, D. Zhao, *ACS Appl. Mater. Interface* 8 (2016) 17268–17275.
- [23] S. Abedi, A. Morsali, *New J. Chem.* 39 (2015) 931–937.
- [24] S. Mosleh, M.R. Rahimi, M. Ghaedi, K. Dashtian, S. Hajati, *RSC Adv.* 6 (2016) 17204–17214.
- [25] Y. An, H. Li, Y. Liu, B. Huang, Q. Sun, Y. Dai, X. Qin, X. Zhang, *J. Solid State Chem.* 233 (2016) 194–198.
- [26] T. Araya, M. Jia, J. Yang, P. Zhao, K. Cai, W. Ma, Y. Huang, *Appl. Catal. B-Environ.* 203 (2017) 768–777.
- [27] Q. Qi, S. Liu, X. Li, C. Kong, Z. Guo, L. Chen, *J. Solid State Chem.* 255 (2017) 108–114.
- [28] A.N. Okte, D. Karamanis, E. Chalkia, D. Tuncel, *Mater. Chem. Phys.* 187 (2017) 5–10.
- [29] G. Zhu, X. Li, H. Wang, L. Zhang, *Catal. Commun.* 88 (2017) 5–8.
- [30] Y. Song, Y. Chen, J. Wu, Y. Fu, R. Zhou, S. Chen, L. Wang, *J. Alloys Compd.* 694 (2017) 1246–1253.
- [31] Y. Zou, Z. Qi, Z. Ma, W. Jiang, R. Hu, J. Duan, *J. Electroanal. Chem.* 788 (2017) 184–191.
- [32] X. Yang, L. Qiu, X. Luo, *RSC Adv.* 8 (2018) 4890–4894.
- [33] X. Zhao, J. Feng, J. Liu, J. Lu, W. Shi, G. Yang, G. Wang, P. Feng, P. Cheng, *Adv. Sci.* 5 (2018).
- [34] S. Chen, J. Yu, J. Zhang, *J. CO₂ Util.* 24 (2018) 548–554.
- [35] L. Pan, T. Muhammad, L. Ma, Z.-F. Huang, S. Wang, L. Wang, J.-J. Zou, X. Zhang, *Appl. Catal. B-Environ.* 189 (2016) 181–191.
- [36] M. Rad, S. Dehghanpour, *RSC Adv.* 6 (2016) 61784–61793.
- [37] M. Gustafsson, A. Bartoszewicz, B. Martin-Matute, J. Sun, J. Grins, T. Zhao, Z. Li, G. Zhu, X. Zou, *Chem. Mater.* 22 (2010) 3316–3322.
- [38] S. Zhou, Y. Wei, J. Hou, L.-X. Ding, H. Wang, *Chem. Mater.* 29 (2017) 7103–7107.
- [39] C. Lin, S.S. Shinde, Z. Jiang, X.K. Song, Y. Sun, L.L. Guo, H. Zhang, J.Y. Jung, X.P. Li, J.H. Lee, *J. Mater. Chem. A* 5 (2017) 13994–14002.
- [40] F.E. Li, C.X. Duan, H. Zhang, X. Yan, J.Q. Li, H.X. Xi, *Ind. Eng. Chem. Res.* 57 (2018) 9136–9143.
- [41] T. Loiseau, C. Serre, C. Huguenard, G. Fink, F. Taulelle, M. Henry, T. Bataille, G. Ferey, *Chem. Eur. J.* 10 (2004) 1373–1382.
- [42] H. Wang, X. Yuan, Y. Wu, G. Zeng, X. Chen, L. Leng, Z. Wu, L. Jiang, H. Li, J. Hazard. Mater. 286 (2015) 187–194.
- [43] S.K. Wu, X.P. Shen, G.X. Zhu, H. Zhou, Z.Y. Ji, K.M. Chen, A.H. Yuan, *Appl. Catal. B-Environ.* 184 (2016) 328–336.
- [44] G. Kresse, D. Joubert, *Phys. Rev. B* 59 (1999) 1758–1775.
- [45] G. Kresse, J. Furthmuller, *Comp. Mater. Sci.* 6 (1996) 15–50.
- [46] J.P. Perdew, K. Burke, M. Ernzerhof, *Phys. Rev. Lett.* 77 (1996) 3865–3868.
- [47] S.L. Dudarev, G.A. Botton, S.Y. Savrasov, C.J. Humphreys, A.P. Sutton, *Phys. Rev. B* 57 (1998) 1505–1509.
- [48] S. Lany, H. Raebiger, A. Zunger, *Phys. Rev. B* 77 (2008) 241201–241204.
- [49] F. Jeremias, V. Lozan, S.K. Henninger, C. Janiak, *Dalton Trans.* 42 (2013) 15967–15973.
- [50] Y. Zhang, Q. Gao, Z. Lin, T. Zhang, J. Xu, Y. Tan, W. Tian, L. Jiang, *Sci. Rep.* 4 (2014) 4947–4952.
- [51] S. Friebe, A. Mundstock, D. Unruh, F. Renz, J. Caro, *J. Membr. Sci.* 516 (2016) 185–193.
- [52] K. Zhu, Y. Liu, J. Liu, *RSC Adv.* 4 (2014) 42278–42284.
- [53] P. George, N.R. Dhabarde, P. Chowdhury, *Mater. Lett.* 186 (2017) 151–154.
- [54] Y. Fu, D. Sun, Y. Chen, R. Huang, Z. Ding, X. Fu, Z. Li, *Angew. Chem. Int. Ed.* 51

(2012) 3364–3367.

[55] L. Liu, X. Tai, N. Zhang, Q. Meng, C. Xin, *React. Kinet. Mech. Catal.* 119 (2016) 335–348.

[56] G. Zi, Z. Yan, Y. Wang, Y. Chen, Y. Guo, F. Yuan, W. Gao, Y. Wang, J. Wang, *Carbohydr. Polym.* 115 (2015) 146–151.

[57] B. Li, J. Liu, Z. Nie, W. Wang, D. Reed, J. Liu, P. McGrail, V. Sprenkle, *Nano Lett.* 16 (2016) 4335–4340.

[58] G. Ferey, C. Serre, *Chem. Soc. Rev.* 38 (2009) 1380–1399.

[59] X.G. Han, H.Z. He, Q. Kuang, X. Zhou, X.H. Zhang, T. Xu, Z.X. Xie, L.S. Zheng, *J. Phys. Chem. C* 113 (2009) 584–589.

[60] M.J. Cao, F. Wang, J.F. Zhu, X. Zhang, Y. Qin, L. Wang, *Mater. Lett.* 192 (2017) 1–4.

[61] D. Sengupta, B. Mondal, K. Mukherjee, *J. Nanopart. Res.* 19 (2017) 100–112.

[62] F. Zhang, H. Cao, D. Yue, J. Zhang, M. Qu, *Inorg. Chem.* 51 (2012) 9544–9551.

[63] L.X. Yin, D.D. Zhang, J. Wang, J.F. Huang, X.G. Kong, J.M. Fang, F. Zhang, *Mater. Charact.* 127 (2017) 179–184.

[64] S. Wang, P. Kuang, B. Cheng, J. Yu, C. Jiang, *J. Alloys. Compd.* 741 (2018) 622–632.

[65] J. Xu, Y. Chang, Y. Zhang, S. Ma, Y. Qu, C. Xu, *Appl. Surf. Sci.* 255 (2008) 1996–1999.

[66] Y.G. Zhang, L.L. Ma, J.L. Li, Y. Yu, *Environ. Sci. Technol.* 41 (2007) 6264–6269.

[67] T.V.L. Thejaswini, D. Prabhakaran, M.A. Maheswari, *J. Mater. Sci.* 51 (2016) 8187–8208.

[68] Z.M. Liu, Y.C. Wu, J.T. Chen, Y.R. Li, J.Y. Zhao, K.H. Gao, P. Na, *Catal. Sci. Technol.* 8 (2018) 1936–1944.

[69] H.J. Lee, J.H. Kim, S.S. Park, S.S. Hong, G.D. Lee, *J. Ind. Eng. Chem.* 25 (2015) 199–206.

[70] G. Liu, P. Niu, C.H. Sun, S.C. Smith, Z.G. Chen, G.Q. Lu, H.M. Cheng, *J. Am. Chem. Soc.* 132 (2010) 11642–11648.

[71] Y.C. Zhang, Z. Li, L. Zhang, L. Pan, X.W. Zhang, L. Wang, J. Fazal-e-Aleem, J. Zou, *Appl. Catal. B-Environ.* 224 (2018) 101–108.

[72] N. Li, Y. Tian, J. Zhao, J. Zhang, J. Zhang, W. Zuo, Y. Ding, *Appl. Catal. B-Environ.* 214 (2017) 126–136.

[73] X.B. Chen, L. Liu, P.Y. Yu, S.S. Mao, *Science* 331 (2011) 746–750.

[74] T. Jan, J. Iqbal, M. Ismail, Q. Mansoor, A. Mahmood, A. Ahmad, *Appl. Surf. Sci.* 308 (2014) 75–81.

[75] N.A. Putri, V. Fauzia, S. Iwan, L. Roza, A.A. Umar, S. Budi, *Appl. Surf. Sci.* 439 (2018) 285–297.

[76] T. Jan, J. Iqbal, M. Ismail, A. Mahmood, *J. Appl. Phys.* 115 (2014) 154308.

[77] P.F. Gu, X.D. Wang, T. Li, H.M. Meng, *Appl. Surf. Sci.* 48 (2013) 4699–4703.

[78] M. Sima, M. Baibarac, E. Vasile, M. Sima, L. Mihut, *Appl. Surf. Sci.* 355 (2015) 1057–1062.

[79] P. Jakes, E. Erdem, *Phys. Status Solidi-RRL* 5 (2011) 56–58.

[80] Z. Wang, K. Wang, H. Wang, X. Chen, W. Dai, X. Fu, *Catal. Sci. Technol.* 8 (2018) 3260–3277.

[81] X. Yu, W. Li, Z.H. Li, J.W. Liu, P.A. Hu, *Appl. Catal. B-Environ.* 217 (2017) 48–56.

[82] X. Lv, Y. Du, Z. Li, Z. Chen, K. Yang, T. Liu, C. Zhu, M. Du, Y. Feng, *Vacuum* 144 (2017) 229–236.

[83] J. Kaur, S. Singhal, *Ceram. Int.* 40 (2014) 7417–7424.

[84] A.N. Kadam, T.G. Kim, D.S. Shin, K.M. Garadkar, J. Park, *J. Alloys Compd.* 710 (2017) 102–113.

[85] C. Yan, Z. Lina, N. Lichao, Z. Congjie, Z. Hua, L. Bin, Y. Heqing, *Chem. Eng. J.* 264 (2015) 557–564.

[86] D. Yolacan, N.D. Sankir, *J. Alloys Compd.* 726 (2017) 474–483.

[87] A.N. Kadam, D.P. Bhopate, V.V. Kondalkar, S.M. Majhi, C.D. Bathula, A.V. Tran, S.W. Lee, *J. Ind. Eng. Chem.* 61 (2018) 78–86.